Computing and Visualization in Science manuscript No.
(will be inserted by the editor)

A Parallel Algebraic Multigrid Solver for Finite Element Method based Source Localization in the Human Brain ⋆

C.H. Wolters[1,3], M. Kuhn[2], A. Anwander[3], S. Reitzinger[2]

[1] Max Planck Institute for Mathematics in the Sciences, Leipzig, Germany, http://www.mis.mpg.de
[2] SFB F013 "Numerical and Symbolic Scientific Computing", Johannes Kepler University Linz, Austria, http://www.sfb013.uni-linz.ac.at
[3] Max Planck Institute of Cognitive Neuroscience, Leipzig, Germany, http://www.cns.mpg.de

The correct dates will be entered by Springer

Abstract Time plays an important role in medical and neuropsychological diagnosis and research. In the field of Electro- and MagnetoEncephaloGraphy (EEG/MEG) source localization, a current distribution in the human brain is reconstructed noninvasively by means of measured fields outside the head. High resolution finite element modeling for the field computation leads to a sparse, large scale, linear equation system with many different right hand sides to be solved. The presented solution process is based on a parallel algebraic multigrid method. It is shown that very short computation times can be achieved through the combination of the multigrid technique and the parallelization on distributed memory computers. A solver time comparison to a classical parallel Jacobi preconditioned conjugate gradient method is given.

Key words EEG/MEG-source localization in the human brain, Algebraic multigrid, Parallel iterative solvers.

1 Introduction

Nowadays devices and tools are available for analyzing and monitoring the human brain with fine details. These details are necessary, e.g., for successful surgery or, more generally, for basic brain research. Often computational methods are used in the diagnosis- and pre-surgical phase. Such non-invasive tools are of course preferable to invasive methods, e.g., surgery, with high risks for patients. In basic human brain research, most often there is no other choice besides computational methods. However, the acceptance of tools depends very much on their speed and their reliability and robustness. In this paper it will be shown how advanced numerical methods enhance such tools or make them work at all. The paper brings together clinical diagnosis, pre-surgical planning, clinical and cognitive research and numerical mathematics, and describes the requirements of necessary algorithms and software.

It is normal practice in cognitive research and in clinical routine and research to localize current sources in the human brain by means of the induced electric potentials, measured with electrodes which are fixed on the scalp (EEG) and/or the induced magnetic fluxes, measured in a distance of a few centimeters from the head surface (MEG). The localization of the underlying source distribution is an *inverse problem* whose solution requires the repeated simulation of the electric/magnetic propagation in the head for a varying source in the brain (*forward problem*). During the forward problem, the volume-conductor head has to be modeled. An overview about the head tissues with different conductivities can be found in Haueisen et al. [20]. The human skull, e.g. is an inhomogeneously conducting layer which consists of different plates with suture lines in between. These inhomogeneities have an influence on the inverse source localization, as shown by Pohlmeier et al. [35]. Van den Broek et al. [45] reported a large influence of holes in the skull or lesions in the brain to the field simulations. If the skull, from a macroscopic point of view, is regarded as one unit consisting of a soft bone layer (spongiosa) enclosed by two hard bone layers (compacta), its conductivity shows an anisotropy with a ratio of about 1:10 (radially:tangentially to the skull surface) (Akhtari et al. [1]). First results show that neglecting this anisotropy in the forward problem can lead to spurious errors in the

Send offprint requests to: *Carsten Wolters, MPI für neuropsychologische Forschung, MEG-Gruppe, Muldentalweg 9, 04828 Bennewitz, Germany, E-mail: wolters@cns.mpg.de.*

⋆ *Acknowledgements: We would like to thank Prof.W.Dahmen, director of the Institute for Geometry and Practical Mathematics, RWTH Aachen. This work has been supported by Prof.E.Zeidler, director of the MPI for Mathematics in the Sciences Leipzig, by the Leibniz-Prize of the German Research Foundation awarded to Prof.A.D.Friederici, director of the MPI of Cognitive Neuroscience Leipzig, by the Austrian Science Fund – 'Fonds zur Förderung der wissenschaftlichen Forschung' – within the SFB F013 "Numerical and Symbolic Scientific Computing", and by the IST-program of the European Commission, project No.10378, SimBio.*

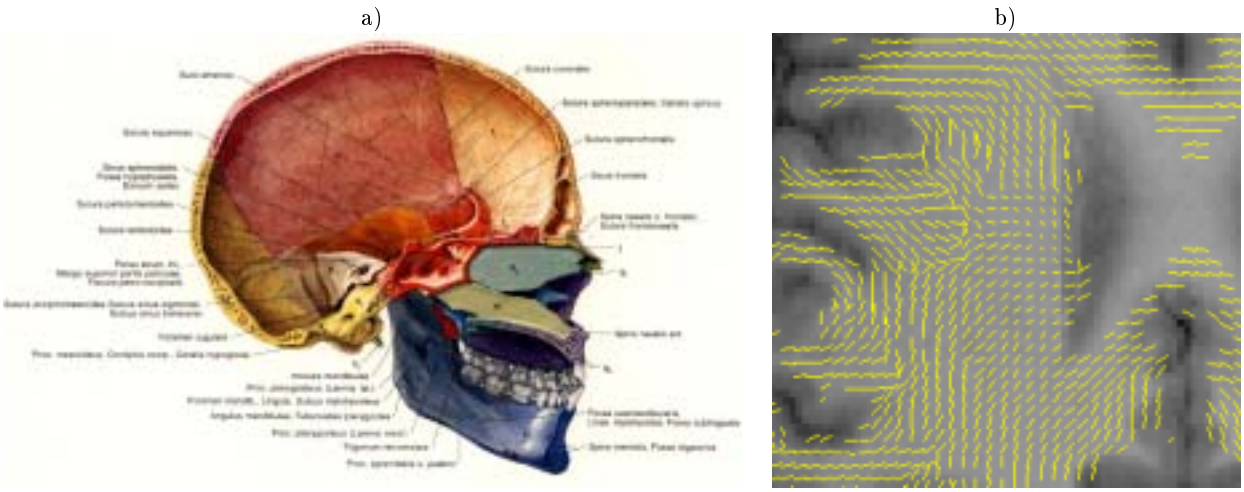

Figure 1. *Head geometry: a) The human skull: Suture lines and the tri-layeredness, Platzer [33]. b) Diffusion Tensor Imaging reveals anisotropy of brain white matter, Wolters et al. [53].*

inverse current reconstruction result (Marin et al. [30]). An anisotropic conductivity with a ratio of 1:9 (normal:parallel to fibers) has been measured for brain white matter. Figure 1, taken from Platzer [33] and Wolters et al. [53], illustrates geometrical features of skull and white matter tissues. Models and measurement techniques to approximate and include white matter anisotropy into source localization procedures can be found in [21; 44; 53]. Haueisen et al. [21] presented a first study showing a non neglectable influence of white matter conductivity anisotropy to the forward problem.

A bottleneck for sensitivity-studies of tissue inhomogeneities/anisotropies towards the different inverse source reconstruction techniques and especially for broad application of high resolution volume conductor modeling to inverse reconstructions in the application fields is the time for calculating the 3D potential distributions during the various forward problems that have to be solved. Waberski et al. [46], e.g., conclude that for the achievement of the final goal in epilepsy source localization, i.e., the general clinical use, high resolution realistically shaped head models are necessary and parallel computing has to speed the computation. Finite element (FE) models for the electromagnetic field simulation in the head have been developed by various research-groups (see e.g. [5; 20; 45; 7; 3; 30]). The FE method is able to treat geometries of arbitrary shape, inhomogeneous and anisotropic conductivities. Generally iterative solvers like the preconditioned Conjugate Gradient (CG) method with conventional preconditioners on single processor machines have been used for the large linear equation system arising from this approach. The hundred or even thousand times repeated solution of such a system with a constant stiffness matrix and varying right hand sides is the major time consuming part within the inverse localization process. These calculation times limited the resolution of the models or, even stronger, the broader application of FE based head modeling to practical source localization problems got stuck.

Geometric MultiGrid (GMG) methods have proven to be of optimal order with respect to memory requirement and arithmetic costs, see e.g. Hackbusch [19]. In Jung and Langer [24], it was shown that multigrid methods are efficient preconditioners for the conjugate gradient method. For a parallel implementation see for instance Bastian et al. [4]. GMG suffer from the requirement of a grid hierarchy, which is not available in our case. By contrast, Algebraic MultiGrid (AMG) methods use only single grid information (see e.g. [37; 6; 26; 17] and for parallel versions [13; 28; 16; 47]) while mostly preserving the properties of the geometric version. Many numerical studies have shown a good performance of AMG preconditioners. Furthermore, AMG preconditioners were successfully applied to source localization recently ([50; 23]). Even if AMG preconditioned CG (AMG-CG) was shown to be very fast in comparison to standard methods, additional speedup is required. This paper describes how the latter can be achieved for realistically shaped high resolution head models by using a parallel computer with a moderate number of processors.

Subsection 1.1 of this paper will give an overview about different application fields of source localization and will present an exemplary reconstruction result for Somatosensory Evoked Potentials (SEP). The subsection is meant to be a further motivation for interested readers not stemming from the bioelectromagnetism area and it can be skipped otherwise. In Section 2, the modeling aspects for the forward problem will be described. An overview about a physical model for the source and for the field propagation in the head volume conductor will be presented. A short introduction to the automatic generation of realistically shaped high resolution head models using multimodal Magnetic Resonance Imaging (MRI) based segmentation and tetrahedral and cubic FE meshing will then be given. The section terminates with an FE formulation. In Section 3, the AMG-CG solver will be introduced as a fast solver for the large linear

equation system arising from the FE approach. The partitioning of the meshes and a parallelization strategy for distributed memory computers will then be presented. Section 4 describes the new software developments, necessary for the achievement of the results in Section 5, where numerical studies will be presented within realistically shaped high resolution head models. The parallelized multigrid method will be compared with a parallel Jacobi-preconditioned CG method (Jacobi-CG), which is a well-known solver method in FE source localization. It will be shown that high speedups can be achieved which open the possibility for a broader application of high resolution FE based source localization in the human brain. The paper ends with the discussion of the results and the conclusions in Section 6.

1.1 Overview about applications of source localization

This subsection is only meant to be a further motivation and to list some references for readers who would like to know more about the inverse problem and some well-established application fields of EEG/MEG-source localization.

An overview about the different application fields of source localization can be found in Andrä and Nowak [2]. Various inverse reconstruction techniques for continuous and discrete source parameter spaces are described, e.g., in [38; 7; 27; 48; 52; 39; 40].

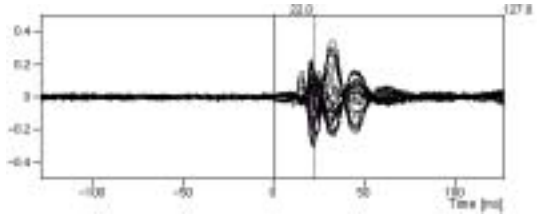

Figure 2. *SEP example dataset, taken from CURRY: Butterfly plot of averaged EEG data from* -0.4 *to* $0.4\ \mu V$*. The P22 signal component is marked.*

A first example is the study of functional cortical organization by means of evoked fields of the somatosensory system. The different evoked signal components of interest in such studies appear during the first 100 ms poststimulus. Since the components are well time-locked and not dependent on the attention of the subjects, the signal-average can be built over a large number of trials so that the signal components of interest are equipped with a relatively good signal-to-noise ratio. Figure 2 shows the averaged EEG measurements for SEP in 31 channel butterfly plot from Fuchs et al. [14], included as an example dataset in the software package CURRY [11]. To give an impression for a medically interesting source localization result, the continuous dipole fit method, introduced by Scherg and von Cramon [38], with two dipoles at the peak of the SEP-P22 signal component is shown in Figure 3 (see Fuchs et al. [14]). The result has been calculated using the example dataset and methods within CURRY [11]. Source localization methods have also been introduced to characterize the generators of signals related to higher cognitive function. An example is a recent study showing equivalences between speech and music processing in the brain (Maess et al. [29]).

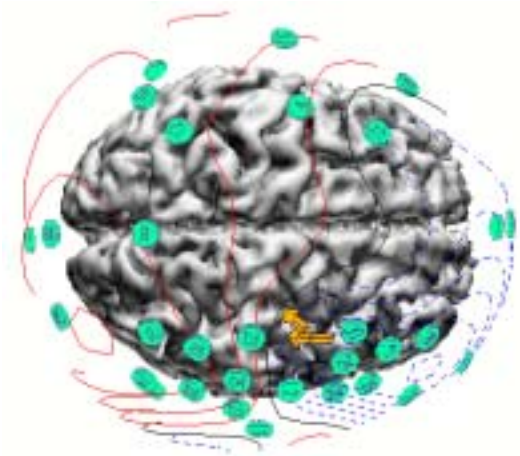

Figure 3. *SEP source localization example, computed with CURRY [11]: Results of the continuous dipole fit method with two dipoles at the peak of the P22 signal component.*

The non-invasive EEG/MEG-source localization diagnosis method is successfully used in clinical research and application. For instance tumors may distort brain anatomy so that the presurgical localization of sensory or motor areas on the basis of anatomical landmarks is impossible. In Sutherling et al. [43], the agreement between invasive and the non-invasive diagnosis method have been evaluated and an "excellent precision of the source localization results" was found. About 0.25 % of the world population suffers from drug-resistant epilepsy and about 10 to 15 % would profit from a surgical removement of the epileptogenic tissue [2]. As opposed to alternative invasive diagnostic procedures, i.e., opening the skull and implanting electrodes near the assumed focus (ECoG surface electrodes or depth electrodes) which put the patient under a considerable risk and is cost intensive, source localization procedures are non-invasive and can give a more "global" overview since the sensors can be placed around the whole head. Waberski et al. [46], e.g., found a high congruence of source reconstruction and invasive determination of the focus of epileptiform activity using realistically shaped head models.

2 The forward problem

2.1 Physical modeling

The sources to be localized during the inverse problem and to be modeled in the forward problem are elec-

trolytic currents within the dendrites of the large pyramidal cells of activated neurons in the cortex sheet of the human brain. A stimulus-induced activation of a large number of excitatory synapses of a whole pattern of neurons leads to a negative monopole under the brain surface, whereas the cells in rest form a positive monopole quite closely underneath. Such a stimulus can have various forms, e.g., any visual or auditory stimulus in neuropsychological experiments or an epilepsy- or tumor-induced stimulus as clinical examples. The resulting primary current is generally formulated as a mathematical dipole

$$\mathbf{j}^p(\mathbf{x}) = \mathbf{M}\delta_{\mathbf{x}_0}(\mathbf{x}) \tag{1}$$

at the position $\mathbf{x}_0$ with the moment $\mathbf{M}$ (see, e.g., Nunez [31]). The dipole source establishes an electric field $\mathbf{E}$ and a return current $\sigma\mathbf{E}$ in the whole head with σ a 3×3 conductivity tensor. The total current distribution $\mathbf{j}$ in the head is then modeled as

$$\mathbf{j} = \mathbf{j}^p + \sigma\mathbf{E}.$$

Since in the considered low frequency band, the capacitive component of tissue impedance and the electromagnetic propagation effect can be neglected (Plonsey and Heppner [34]), the fields are quasistatic and $\mathbf{E}$ can be expressed as the negative gradient of a scalar potential u, so that

$$\mathbf{j} = \mathbf{j}^p - \sigma\nabla u.$$

Because the divergence of $\mathbf{j}$ must be zero, we arrive at the quasistatic approach of Maxwell's equations of electrodynamics

$$\nabla\cdot(\sigma\nabla u) = J^p = \nabla\cdot\mathbf{j}^p \quad \text{in } \Omega \tag{2}$$

with appropriate boundary conditions

$$\sigma\frac{\partial u}{\partial\mathbf{n}}\bigg|_{\Gamma} = 0 \tag{3}$$

with Ω the head, Γ the head surface and $\mathbf{n}$ the surface normal. Additionally, a reference electrode with given potential is assumed, i.e.,

$$u_{ref} = 0\,. \tag{4}$$

If the scalar potential is known, the magnetic flux through an MEG-magnetometer can then be calculated using a corollary from Biot-Savart's law (see, e.g., Wolters et al. [53]).

The subtraction method (see, e.g., Awada et al. [3]) splits the total potential u into two parts, the singularity potential u^∞ and the correction potential u^{corr}

$$u = u^\infty + u^{corr}. \tag{5}$$

The singularity potential is the solution for a current dipole in an unbounded homogeneous conductor with constant conductivity σ_0 (the isotropic conductivity value at the dipole location x_0),

$$u^\infty(\mathbf{x}) = \frac{1}{4\pi\sigma_0}\frac{\mathbf{M}(\mathbf{x}-\mathbf{x}_0)}{|\mathbf{x}-\mathbf{x}_0|^3},$$

which can be computed very fast. Subtracting the differential equation for the singularity potential from equation (2) yields the following equation for the correction potential

$$\nabla\cdot(\sigma\nabla u^{corr}) = -\nabla\cdot((\sigma-\sigma_0)\nabla u^\infty) \quad \text{in } \Omega \tag{6}$$

and the inhomogeneous Neumann boundary conditions at the surface

$$\sigma\frac{\partial u^{corr}}{\partial\mathbf{n}}\bigg|_{\Gamma} = -\,\sigma\frac{\partial u^\infty}{\partial\mathbf{n}}\bigg|_{\Gamma}. \tag{7}$$

When solving this towards u^{corr}, the unknown scalar potential u can then be calculated using equation 5.

De Munck and Peters [12] derived series expansion formulas for problem (2) with boundary conditions (3) and reference potential (4) in order to calculate the potential distribution for a dipolar source in a multi-layer spherical shell model with constant isotropic or anisotropic conductivity values/tensors within each layer. It is now widely known that realistically shaped models of the human head are needed to minimize the localization error (see, e.g., Waberski et al. [46]).

2.2 Generation of a realistic 5 tissue head model

A prerequisite for a realistic modeling of the volume conductor is the segmentation of head tissues with different conductivity properties. The exact modeling of the low-conducting human skull is of special importance for EEG/MEG-source localization (Huiskamp et al. [22]). The skull can be seen as an isolating layer which leads to a strong decrease and a blurring of the potential distribution towards the measurement electrodes. MRI is known as a save and non-invasive method for imaging the human head. The identification of the CerebroSpinal Fluid(CSF)-skull boundary based on T1-MRI (T1-weighted MRI) is problematic, and PD-MRI (proton-density-weighted MRI) is most appropriate for this task (see Figure 4). A strong segmentation improvement of the CSF-skull boundary could be achieved

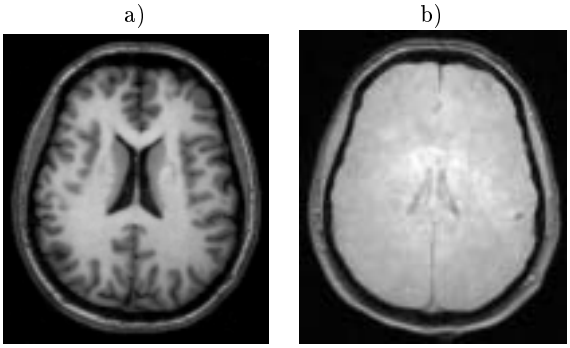

Figure 4. *Axial slices of a a) T1-weighted MRI b) registered proton-density-weighted MRI.*

through the exploitation of the registered PD image. When compared to procedures, solely based on a T1 image modality, where the segmented brain surface is smoothed and dilated in order to estimate the inner skull, larger errors in areas of the skull base, but also at the neurocranial roof, where the CSF layer between brain and skull is underestimated, are reported in [8; 22; 49]. Errors in EEG source localization of up to 1cm in mesial-temporal and basal-frontal regions, resulting from inaccurate skull segmentation, were found in Huiskamp et al. [22]. The segmentation of outer skull, skin, white and gray matter surfaces was carried out as described in Wolters [49], resulting in the 5-tissue head model, shown in Figure 5. In future studies, the

Figure 5. *Cut through an axial layer of the 5-tissue segmentation result through multimodal MR-imaging.*

skull conductivity tensor eigenvectors will be automatically determined by means of the triangle normals of a deformable model within the skull spongiosa space and Diffusion Tensor Imaging (DTI) methods will be used to measure/model the conductivity anisotropy of the white matter as shown in Figure 1 and described in [21; 44; 53; 49].

2.3 Discretization and Mesh Generation

Numerical methods are needed for field simulations in volume conductors which exploit individual tissue segmentation results. Within this paper, we will use the FE method and equation (2) will be discretized, using a direct approach. Therefore, the *blurred dipole* model has been introduced for FE based source localization in Buchner et al. [7], which will be shortly summarized now. The blurred dipole is made up from monopole sources $J_k^b := J^b(\mathbf{x}_k)$, calculated for all neighboring FE mesh nodes $\mathbf{x}_k$ around the location $\mathbf{x}_i$ of a mathematical dipole $\mathbf{M}_i := \mathbf{M}\delta_{\mathbf{x}_i}(\mathbf{x})$, so that

$$D = \frac{1}{2}\left({}^{n_0}\mathbf{M}_i^r - (\Delta\bar{\mathbf{x}}_{ki}^r)^{n_0} J_k^b\right)\left({}^{n_0}\mathbf{M}_i^r - (\Delta\bar{\mathbf{x}}_{si}^r)^{n_0} J_s^b\right) + \lambda\frac{1}{2} J_k^b g_{ks} J_s^b \stackrel{!}{=} min$$

$$g_{ks} := \begin{cases} (\Delta\bar{\mathbf{x}}_{ki}^r \Delta\bar{\mathbf{x}}_{si}^r)^{n_s/2} & if\ k = s \\ 0 & if\ k \neq s \end{cases}$$

with $\Delta\bar{\mathbf{x}}_{ki}^r = \Delta\mathbf{x}_{ki}^r/a$ the r-component of the a-weighted vector from node i to node k, $\Delta\mathbf{x}_{ki}$, n_0 the order of the source model and n_s the dipole smoothness. The first part of the functional D ensures a minimal difference between the resultant moment of the blurred dipole and the one of the mathematical dipole, while the second part, a Tikhonov-Phillips regularizer, smoothes the monopole distribution and enables a unique minimum for D. The differentiation of D with respect to J^b expresses the condition for the minimum and a linear system of equations is established.

$$\left[(\Delta\bar{\mathbf{x}}_{ki}^r)^{n_0}(\Delta\bar{\mathbf{x}}_{si}^r)^{n_0} + \lambda g_{ks}\right] J_s^b = (\Delta\bar{\mathbf{x}}_{ki}^r)^{n_0}\,\mathbf{M}_i^{n_0} \qquad (8)$$
$$\sum_k J_k^b = 0$$

Together with $J_t^b = 0$ for all non-neighbor indices t of dipole index i, the monopole distribution of the blurred dipole model is defined. See Buchner et al. [7] for a motivation of this source model and for accuracy tests in a sphere model, where the numerical results were compared with results of an analytical formula from Smythe [42] for two closely neighbored monopoles, a source and a sink. The direct application of variational and FE techniques to equation (2) with boundary conditions (3) together with the blurred dipole model yields a system of linear equations

$$\mathsf{K}_h \underline{u}_h = \underline{\mathsf{J}}_h \qquad (9)$$

with $\mathsf{K}_h \in \mathbb{R}^{N_h \times N_h}$ the stiffness matrix, $\underline{\mathsf{J}}_h \in \mathbb{R}^{N_h}$ the source load and $\underline{u}_h \in \mathbb{R}^{N_h}$ the solution vector for the total potential. The stiffness matrix is given by

$$\mathsf{K}_h^{[i,j]} = \int_\Omega \nabla\psi_j \sigma \nabla\psi_i \, d\Omega \qquad (10)$$

and the right hand side entries for the direct method by

$$\left[\underline{\mathsf{J}}_h\right]^i = -\int_\Omega J_i^b \psi_i \, d\Omega \qquad (11)$$

for an FE-basis $\mathbb{V}_h = span\{\psi_i\}_{i=1}^{N_h}$. The subindex h denotes the average meshsize and $N_h = O(h^{-3})$ is the number of unknowns as h tends to zero. The condition number of the stiffness matrix behaviors asymptotically like $O(h^{-2})$.

The subtraction method (6,7) leads to an equation system $\mathsf{K}_h \underline{u}_h^{corr} = \underline{\mathsf{J}}_h^\infty$ with the same stiffness matrix (10), but with the right hand side entries

$$\left[\underline{\mathsf{J}}_h^\infty\right]^i = -\sum_{j=1}^{N_h}\left[\int_\Omega \nabla\psi_j\,(\sigma - \sigma_0)\,\nabla\psi_i d\Omega + \int_\Gamma \sigma_0 \langle\nabla\psi_j, \mathbf{n}\rangle \psi_i d\Gamma\right] u_j^\infty.$$

The solution vector $\underline{u}_h^{corr}$ is the FE approximation of the correction potential and equation (5) is used to calculate the total potential. Since the stiffness matrix is the same for the subtraction method and the solvers are independent of the right hand side of the equation system, the

results presented in the following are as well valid for the subtraction method.

An essential prerequisite is the generation of an FE mesh representing the geometric and electric properties of the head volume conductor. Two different approaches have been chosen. The first approach uses a surface-based tetrahedral tessellation of the relevant compartments skin, skull, CSF, brain gray and white matter and ventricular system, described in Wagner [48]. Auxiliary surfaces with a distance d_1 from the given compartment borders are generated so that a set of layered surfaces is obtained. In a next step, the vertices of the tetrahedral mesh are generated by means of a thinning of the surfaces with thinning-distance d_1 for auxiliary and d_2 for compartment surfaces. $d_2 = 2mm$ enabled a very exact representation of the skull-layer. A distance of 1.3 times d_2 was chosen for d_1, since the resolution deeper in the brain was considered to be less important for an appropriate accuracy. This resulted into 119299 nodes. After a three-dimensional Delaunay triangulation, each of the 713733 tetrahedra was labeled according to its compartment. Figure 6 shows the tetrahedra mesh for the 5 tissue

Figure 6. *Tetrahedra mesh of the 5 tissue head model.*

head model. The top part was cutted away in order to enable a view to the inside. The second mesh generation exploits the discretization of 3D space which is a given for any scanned medical dataset. High-resolution 2mm isotropic cube elements have been generated and labeled according to their position as described above. This resulted in a model with 325384 nodes and 307580 elements.

Both FE meshes were generated using the software package CURRY [11].

3 Parallel Algebraic Multigrid Solver

The inverse reconstruction process requires the solution of hundreds or even thousands of large scale systems (9) with the stiffness matrix (10). In Wolters et al. [50], condition numbers of about 10^7 have been calculated for high resolution realistically shaped head stiffness matrices, causing severe accuracy and convergence problems for classical iterative solvers. These problems were recovered by applying appropriate preconditioners for the CG method such that the condition number of the resulting preconditioned stiffness matrix was small. The AMG preconditioner was shown to be superior to incomplete Cholesky factorization with threshold. In Johnson et al. [23], AMG-CG was found to be superior to a successive overrelaxation method.

If we are going to solve the entire localization problem with many calls of the solver, the results cannot be produced within an acceptable time. However, a parallel computer may provide sufficient capacity such that time limitation can be fulfilled. In Haase et al. [16] it has been shown that AMG-CG solvers exhibit high speedups on parallel computers including PC clusters and an SGI ORIGIN 2000. The speedup was especially good for the solver-part of the algorithm. Since the setup of the preconditioner has to be carried out only once per head geometry, its calculation time and speedup can be neglected.

3.1 Algebraic Multigrid Method

As in Geometric MultiGrid (GMG, see Hackbusch [19] for a theoretical overview), the basic idea in AMG is to reduce high and low frequency components of the error by the efficient interplay of smoothing and coarse grid correction, respectively. In AMG, both, the matrix hierarchy and the prolongation operators are constructed just from the stiffness matrix K_h. In analogy, we will speak of "coarse grids" although these are purely virtual and do not have to be constructed explicitly as coarse FE meshes. Since the automatic generation of a grid-hierarchy for GMG and especially the proper assembling of all components would be a very difficult task with respect to conductivity inhomogeneities and anisotropies in a realistically shaped head model, the automatic algebraic construction of a virtual grid is a big advantage. A general concept of AMG methods for FE discretizations can be found in Haase et al. [17]. Each AMG algorithm consists of the following components:

(a) Coarsening: define the splitting $\omega_h = \omega_C \cup \omega_F$ of ω_h (the index set of nodes) into sets of coarse and fine grid nodes ω_C and ω_F, respectively.
(b) Transfer operators: prolongation $\mathfrak{P}_h : V_H \mapsto V_h$ and restriction $\mathfrak{R}_h := \mathfrak{P}_h^T$.
(c) Definition of the coarse matrix by Galerkin's method, i.e., $\mathsf{K}_H := \mathfrak{R}_h \mathsf{K}_h \mathfrak{P}_h$.
(d) Appropriate smoother for the considered problem class.

The most important issue to be discussed is the setup phase, i.e., the construction of the matrix hierarchy and the prolongation operators. We will give the explanation for a two grid method where h is related to the fine grid and H to the coarse grid.

In our case, the stiffness matrix K_h can be associated with an FE grid, i.e., the diagonal entry of the i^{th} row of the matrix K_h is related to a grid point in ω_h and an off-diagonal entry is related to an edge in an FE grid (see

Figure 7). First we look at the coarsening process which

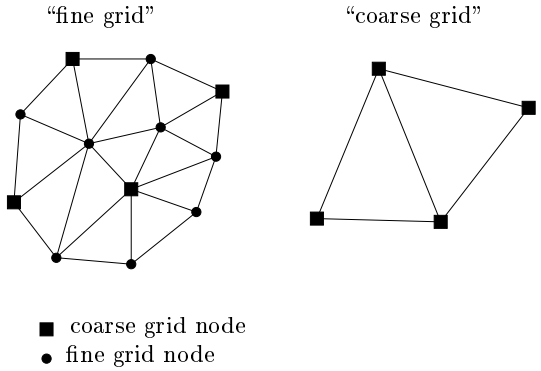

Figure 7. Illustration of a two grid method.

has the task to reduce the nodes such that $N_H = |\omega_C| < N_h = |\omega_h|$. Here, $|\omega|$ denotes the number of elements in the set ω. Motivated from Figure 7, the grid points ω_h can be split into two disjoint subsets ω_C (coarse grid nodes) and ω_F (fine grid nodes), i.e.,

$$\omega_h = \omega_C \cup \omega_F, \quad \omega_C \cap \omega_F = \emptyset$$

such that there are (almost) no direct connections between any two coarse grid nodes and the resulting number of coarse grid nodes is as large as possible. Instead of considering all connections between nodes being of the same rank, we introduce the following sets

$$\begin{aligned} N_h^i &= \left\{ j \mid |\mathsf{K}_h^{[i,j]}| \neq 0,\, i \neq j \right\} \\ S_h^i &= \left\{ j \in N_h^i \mid |\mathsf{K}_h^{[i,j]}| > coarse(i,j,\mathsf{K}_h) \right\} \\ S_h^{i,T} &= \left\{ j \in N_h^i \mid i \in S_h^j \right\} \end{aligned} \tag{12}$$

where N_h^i is the index set of neighbors, S_h^i denotes the index set of nodes with a "strong connection" from node i and $S_h^{i,T}$ is related to the index set of nodes with a "strong connection" to node i (see Ruge and Stüben [37]). In addition $coarse(i,j,\mathsf{K}_h)$ is an appropriate cut-off (coarsening) function, e.g.,

$$coarse(i,j,\mathsf{K}_h) := \alpha \cdot \max_j \{ |\mathsf{K}_h^{[i,j]}| \}\,, \tag{13}$$

with $\alpha \in [0,1]$. With those definitions a splitting into coarse and fine grid nodes can be done. For our computations we used the modified splitting algorithm of Ruge and Stüben [37]. Next the prolongation operator has to be defined correctly. We require that the prolongation operator $\mathfrak{P}_h : V_H \mapsto V_h$ has full rank. There are a lot of possibilities to define such transfer operators with pure algebraic information. For the construction we refer to [37; 6; 26; 47]. A possible setting and the one which turned out to be the most efficient for the presented application is given by

$$(\mathfrak{P}_h)^{[i,j]} = \begin{cases} 1 & i = j \in \omega_C \\ 1/|S_h^{i,T} \cap \omega_C| & i \in \omega_F,\, j \in S_h^{i,T} \cap \omega_C \\ 0 & \text{else}\,. \end{cases} \tag{14}$$

The coarse grid matrix K_H is defined by the classical Galerkin method, i.e.,

$$\mathsf{K}_H = \mathfrak{P}_h^T \mathsf{K}_h \mathfrak{P}_h \ \in \mathbb{R}^{N_H \times N_H}\,,$$

being again symmetric and positive definite (see e.g. Ruge and Stüben [37]).

After the proper definition of the prolongation and coarse grid operators a matrix hierarchy can be setup in a recursive way. Finally, a multigrid cycle can be assembled, see Algorithm 1. Therein the variable CoarseGrid denotes the level where a direct solver is applied.

Algorithm 1 (Parallel) $V(\nu_F,\nu_B)$-cycle $\text{MG}(\mathsf{K}_h, \underline{\mathsf{u}}, \underline{\mathsf{J}})$

if CoarseGrid **then**
  $\underline{\mathsf{u}} \Leftarrow \text{DirectSolve}(\mathsf{K} \cdot \underline{\mathsf{u}} = \underline{\mathsf{J}})$
else
  $\widetilde{\underline{\mathsf{u}}} \Leftarrow \nu_F$ times $\text{Smooth}(\mathsf{K}_h, \underline{\mathsf{u}}, \underline{\mathsf{J}})$
  $\underline{\mathsf{d}} \leftarrow \underline{\mathsf{J}} - \mathsf{K}_h \cdot \widetilde{\underline{\mathsf{u}}}$
  $\underline{\mathsf{d}}^H \leftarrow \mathfrak{P}^T \cdot \underline{\mathsf{d}}$
  $\underline{\mathsf{w}}^H \leftarrow 0$
  $\underline{\mathsf{w}}^H \Leftarrow \text{MG}(\mathsf{K}_H, \underline{\mathsf{w}}^H, \underline{\mathsf{d}}^H)$
  $\underline{\mathsf{w}} \leftarrow \mathfrak{P} \cdot \underline{\mathsf{w}}^H$
  $\widehat{\underline{\mathsf{u}}} \leftarrow \widetilde{\underline{\mathsf{u}}} + \underline{\mathsf{w}}$
  $\underline{\mathsf{u}} \Leftarrow \nu_B$ times $\text{Smooth}^T(\mathsf{K}_h, \widehat{\underline{\mathsf{u}}}, \underline{\mathsf{J}})$
end if

For our application we use AMG-CG, i.e., AMG is applied as a preconditioner for the CG method (see Jung and Langer [24]). For the m-$V(\nu_F,\nu_B)$-cycle AMG preconditioned CG method, the operation $\underline{\mathsf{w}} = \mathsf{C}_K^{-1}\underline{\mathsf{r}}$ is realized by m calls of $\text{MG}(\mathsf{K}_h, \underline{\mathsf{w}}, \underline{\mathsf{r}})$. For the Jacobi-preconditioner, it is $\mathsf{C}_K = \mathsf{D}$ with D the diagonal of K_h. The Preconditioned CG (PCG) method is shown in Algorithm 2.

Algorithm 2 (Par.) PCG algorithm $\text{PCG}(\mathsf{K}_h, \underline{\mathsf{u}}, \underline{\mathsf{J}}, \mathsf{C}_K)$

$\underline{\mathsf{r}} \leftarrow \underline{\mathsf{J}} - \mathsf{K}_h \underline{\mathsf{u}}$
$\underline{\mathsf{w}} \Leftarrow \mathsf{C}_K^{-1} \cdot \underline{\mathsf{r}}$
$\underline{\mathsf{s}} \leftarrow \underline{\mathsf{w}}$
$\gamma \Leftarrow \langle \underline{\mathsf{w}}, \underline{\mathsf{r}} \rangle$
repeat
  $\underline{\mathsf{v}} \leftarrow \mathsf{K}_h \cdot \underline{\mathsf{s}}$
  $\alpha \Leftarrow \gamma / \langle \underline{\mathsf{s}}, \underline{\mathsf{v}} \rangle$
  $\underline{\mathsf{u}} \leftarrow \underline{\mathsf{u}} + \alpha \underline{\mathsf{s}}$
  $\underline{\mathsf{r}} \leftarrow \underline{\mathsf{r}} - \alpha \underline{\mathsf{v}}$
  $\underline{\mathsf{w}} \Leftarrow \mathsf{C}_K^{-1} \cdot \underline{\mathsf{r}}$
  $\gamma \Leftarrow \langle \underline{\mathsf{w}}, \underline{\mathsf{r}} \rangle$
  $\beta \leftarrow \gamma / \gamma_{\text{OLD}}\ ,\ \gamma_{\text{OLD}} \leftarrow \gamma$
  $\underline{\mathsf{s}} \leftarrow \underline{\mathsf{w}} + \beta \underline{\mathsf{s}}$
until termination

3.2 Data Partitioning

The aim of parallelization is to split both data and operations to the P processors available. The consistency of the algorithms is preserved by message passing. In our case, the parallelization is based on a non-overlapping domain decomposition, i.e., we decompose $\overline{\Omega}$ into P subdomains $\overline{\Omega}_s$ such that

$$\overline{\Omega} = \bigcup_{s=1}^{P} \overline{\Omega}_s$$

with

$$\Omega_s \cap \Omega_q = \emptyset \quad \forall q \neq s, \quad s, q = 1, \ldots, P$$

holds. Each subdomain Ω_s is discretized by a mesh $\tau_{h,s}$ such that the whole triangulation

$$\tau_h = \bigcup_{s=1}^{P} \tau_{h,s}$$

of Ω forms a conforming mesh. A global FE space $\mathbb{V}_h$ is defined with respect to τ_h and the local spaces $\mathbb{V}_{h,s}$ are restrictions of $\mathbb{V}_h$ onto $\tau_{h,s}$.

The mesh partitioning of realistic FE geometries with unstructured meshes is critical for the efficiency of the parallel solver method. The distribution must be done so that the number of elements assigned to each processor is the same and the number of adjacent elements assigned to different processors is minimized in order to balance the computation amount among the processors and to minimize the communication between them, respectively. Therefore, graph partitioning algorithms were used which model the FE mesh by a graph (V, E) with vertices V and edges E. Since we are interested in an "element-wise-" in contrast to a "node-wise-" distribution, the dual graph of the FE mesh was partitioned. The finite elements are the vertices of the dual graph and adjacent elements are the corresponding edges. A balanced k-way partitioning was used, minimizing the number of edges which straddle partitions. No weighting of the edges, e.g. with regard to jumping conductivities between elements at tissue-boundaries, was used. The algorithm is based on a multilevel approach, first reducing the size of the dual graph by collapsing vertices and edges, then partitioning the dual graph on the lowest level and further refine during the uncoarsening steps. For the described mesh-partitioning, the software package METIS was used [25]. The results were achieved in a few seconds on a single processor SGI workstation. A first examination of the partitioning result was carried out by means of zooming, rotating, translating, scaling, and applying explosion factors. Figure 8 shows a visualization of the partitioned geometries for 12 processors (see PMVIS [32]). Later, the number of interface and inner nodes and the number of elements were controlled during the calculations. The interface nodes are those nodes which belong to at least two processors, whereas inner nodes only belong to one. In all cases, the quality of the partitioning results were very satisfactory.

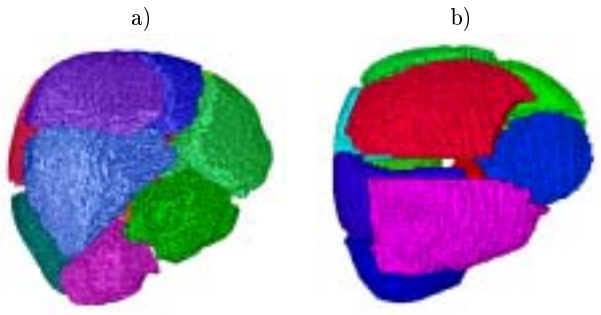

Figure 8. *FE meshes, partitioned for 12 processors with METIS and visualized with PMVIS a) Realistic tetrahedra-head model, 713733 elements b) Realistic cube-head model, 307580 elements.*

3.3 Parallel AMG

The mapping of a vector $\underline{u}_h \in \mathbb{R}^{N_h}$ in global numbering onto a local vector $\underline{u}_s \in \mathbb{R}^{N_s}$ in subdomain $\overline{\Omega}_s$ $(s = 1, \ldots, P)$ is represented symbolically by subdomain connectivity matrices $\mathcal{A}_s : \mathbb{R}^{N_h} \mapsto \mathbb{R}^{N_s}$ with entries

$$\mathcal{A}_s^{[i,j]} := \begin{cases} 1 & \text{if} \quad j = \textsc{Loc2Glob}(i) \\ 0 & \text{else} \end{cases} \qquad \forall i \in \omega_s \,,\ \forall j \in \omega_h$$

where $\textsc{Loc2Glob}(\cdot)$ maps a local index to the global index. The transpose $\mathcal{A}_s^T$ of these binary matrices $\mathcal{A}_s$ maps a local vector back onto the global one. The index set of all those subdomains to which an unknown $u_h^{[j]}$, $j \in \omega_h$ belongs, is denoted by

$$\sigma^{[j]} := \{ s \,|\, u_h^{[j]} \in \overline{\Omega}_s \} \,. \tag{15}$$

We store the data related to the i^{th} node in the subdomain Ω_s if $s \in \sigma^{[i]}$. This approach results in local data denoted by index s of two types (Haase [15]): *accumulated data* (vector $\underline{\mathfrak{u}}$, matrix $\mathfrak{P}$) represented by

$$\underline{\mathfrak{u}}_s := \mathcal{A}_s \cdot \underline{\mathfrak{u}} \,, \qquad \mathfrak{P}_s := \mathcal{A}_s \cdot \mathfrak{P} \cdot \mathcal{A}_s^T \tag{16}$$

and *distributed data* (vector $\underline{\mathsf{d}}$, matrix K_h) represented by

$$\underline{\mathsf{d}} = \sum_{s=1}^{P} \mathcal{A}_s^T \cdot \underline{\mathsf{d}}_s, \qquad \mathsf{K}_h := \sum_{s=1}^{P} \mathcal{A}_s^T \cdot \mathsf{K}_s \cdot \mathcal{A}_s \,. \tag{17}$$

It turns out, that in Algorithms 1 and 2, the functionals are represented as distributed data ($\underline{\mathsf{J}}$, $\underline{\mathsf{v}}$, $\underline{\mathsf{r}}$, $\underline{\mathsf{d}}$, K_h), whereas functions are represented as accumulated data ($\underline{\mathfrak{u}}$, $\underline{\mathfrak{s}}$, $\underline{\mathfrak{w}}$, $\mathfrak{P}$). The local FE accumulation with respect to $\mathbb{V}_{h,s}$ produces automatically distributed matrices K_s. For instance, it can be shown that the multiplication of a distributed matrix K_h with the accumulated vector $\underline{\mathfrak{s}}$ in Algorithm 2 results in a distributed vector $\underline{\mathsf{v}}$:

$$\mathsf{K}_h \cdot \underline{\mathfrak{s}} = \sum_{s=1}^{P} \mathcal{A}_s^T \mathsf{K}_s \mathcal{A}_s \cdot \underline{\mathfrak{s}} = \sum_{s=1}^{P} \mathcal{A}_s^T \left(\mathsf{K}_s \cdot \underline{\mathfrak{s}}_s \right)$$
$$= \sum_{s=1}^{P} \mathcal{A}_s^T \underline{\mathsf{v}}_s = \underline{\mathsf{v}}$$

The realization requires no communication at all because we only have to compute $\underline{\mathsf{v}}_s = \mathsf{K}_s \cdot \underline{\mathfrak{s}}_s$ locally.

If an accumulated matrix $\mathfrak{M}$ fulfills the condition

$$\forall i,j \in \omega_h : \sigma^{[i]} \not\subseteq \sigma^{[j]} \implies \mathfrak{M}^{[i,j]} = 0, \qquad (18)$$

then the operations $\underline{\mathfrak{w}} = \mathfrak{M} \cdot \underline{\mathfrak{w}}^H$, $\underline{\mathfrak{d}}^H = \mathfrak{M}^T \cdot \underline{\mathfrak{d}}$ and $\mathsf{K}_H = \mathfrak{M}^T \mathsf{K}_h \mathfrak{M}$ can be performed locally without any communication (Haase [15]).

In AMG the coarsening and prolongation operators are components which can be chosen. The main idea in the design of parallel AMG is to choose these components such that the resulting prolongation operators $\mathfrak{P}$ are of accumulated type satisfying the pattern condition (18). For this purpose, a local node ordering is introduced by means of a grouping and ordering of the index sets (15) according to $|\sigma^{[j]}|$. The coarsening then starts at interfaces involving more than 2 processors and continues with faces between two processors and finally the coarsening of inner nodes is realized. In addition the coarsening has to be synchronized such that the coarse grid problem is conforming across interfaces between processors. This synchronization requires next neighbor communication. Note that the partitioning of the nodes has only been performed on the finest grid. For a detailed discussion we refer to Haase et al. [16].

Now we observe that Algorithm 1 and Algorithm 2 are also the appropriate parallel formulations, where double-line arrows "$\Leftarrow$" indicate that communication is required for the corresponding operation. In Algorithm 1, the coarse grid system is accumulated globally once in the setup phase. During the iteration only a vector has to be assembled for computing the coarse grid solution. Furthermore, the smoother requires communication and has to be adapted appropriately. We use a Gauss-Seidel smoother for the inner nodes and a Jacobi smoother for the interface nodes. The Jacobi-smoother involves a vector conversion from distributed to accumulated type, i.e., one next neighbor communication across interfaces is required per smoothing step. In this way we get a sophisticated smoother which can be found in Haase [15]. In Algorithm 2, only inner products involve communication besides the preconditioning operation. Since for the inner product of different type vectors it is

$$\begin{aligned}\langle \underline{\mathfrak{w}}, \underline{\mathsf{r}} \rangle &= \underline{\mathfrak{w}}^T \sum_{s=1}^{P} \mathcal{A}_s^T \underline{\mathsf{r}}_s = \sum_{s=1}^{P} (\mathcal{A}_s \underline{\mathfrak{w}})^T \underline{\mathsf{r}}_s \\ &= \sum_{s=1}^{P} \langle \underline{\mathfrak{w}}_s, \underline{\mathsf{r}}_s \rangle,\end{aligned}$$

only one global reduce operation is needed.

4 Software developments

A new FE software package NeuroFEM was developed, based on the package CAUCHY (see [9; 7]). Since it would have been difficult to integrate the FORTRAN77-CAUCHY code using quasistatic memory management in a new C++ class structured inverse toolbox, the old software was redesigned. The inverse toolbox contains a variety of state-of-the-art current source localization methods (SimBio [41], see also [27; 52]). Another argument for the code development was the possibility for a proper interface to the software package PEBBLES including the parallel AMG solver ([36; 16]). The solver code exploits C++ principles of overloading and inheritance.

Therefore, C++ class structured software concepts replace old CAUCHY kernel routines. The storage management within NeuroFEM is fully dynamical so that a recompilation of the software is no longer necessary when changing the problem- and thus memory- size. The new structure facilitated parallel programming on distributed memory computers using the Message-Passing Interface (MPI) standard. The integrated software allows future comparisons with boundary element method based forward simulations (see e.g.[54; 14]) or series expansion formulas in spherical shell models [12].

The coupling to the parallel solver-package is carried out through an "element by element" interface. The root-process determines the index set (15) for each node of the partitioned geometry and scatters the corresponding data together with the material properties to the processors. The arrangement of the nodes to groups according to their index-sets, the ordering of the groups and the allocation of corresponding MPI-communicator groups and the local node numbering is then a fully parallel process. Element-stiffness-matrices are computed on each processor and stored in the local stiffness matrices in FE compact row format. These matrices automatically have the distributed data format (17). The global Dirichlet-node information is scattered to all processors and implemented with a penalty approach in local numbering to those local stiffness matrices whose processor-number is part of the global Dirichlet-node index-set. The coarsening can then be carried out and the hierarchy of stiffness and prolongation matrices can be determined in the parallel setup-phase of the AMG preconditioner as described in Section 3.

5 Results with realistic head models

For the following simulations, one blurred dipolar current source was placed in the somatosensory cortex of the tetrahedra and cube head models. For the parameters of the blurred dipole (see equation (8)), we chose $n_0 = 2$ for the order of the source model, $n_s = 2$ for the dipole smoothness, $\lambda = 10^{-6}$ for the regularization parameter and $a = 20.0$ for the dipole scale, effecting a spatial concentration of monopole loads J_k in the dipole axis around the dipole node. This choice also led to best results in sphere model accuracy tests, when comparing the numerical results with an analytical formula from Smythe [42] for two closely neighbored monopoles, a source and a sink, see Buchner et al. [7]. The zero starting vector $u_0 = \mathbf{0}$ was chosen for the iterative solution process. The FE basis $\mathbb{V}_h$ consisted of piecewise linear

Ansatz-functions. Note that the solver-speed of the algorithms in Section 3 is only dependent on the stiffness matrix (10), so that the following results are valid for both, direct and subtraction method (see Subsections 2.1 and 2.3) and all possible source configurations (i.e., independence of the right-hand side of the linear equation system).

The conductivities σ of skin- and brain-elements were set to 0.33 $[1/\Omega m]$. A conductivity value of 0.0042 $[1/\Omega m]$ was assigned to skull elements and 1.0 $[1/\Omega m]$ to elements in the CSF, i.e., within the layer between brain and skull and within the ventricular system.

The experiment was run on an SGI ORIGIN 2000 with R10000, 195 MHz processors and overall 6GB of main memory. The speedup for 1 up to 12 processors was investigated.

The process of determining the index set (15) for each node and scattering the data to the processors, both carried out by the root, and the local arrangement of nodes to groups according to their index-set and the allocation of corresponding communicator groups takes about half a minute and can be neglected since it has to be done only once per head model.

The solver process was stopped in the i^{th} iteration if the relative error in the controllable $\mathsf{K}_h\mathsf{C}_K^{-1}\mathsf{K}_h$-energy norm was below $\epsilon = 10^{-8}$, i.e.,

$$\frac{\langle \underline{\mathfrak{w}}^i, \underline{\mathfrak{r}}^i \rangle}{\langle \underline{\mathfrak{w}}^0, \underline{\mathfrak{r}}^0 \rangle} \leq \epsilon^2.$$

For the AMG-CG, we used the 1-$V(1,1)$-cycle AMG-preconditioner. Equation (13) was taken as the cut-off coarsening function with $\alpha = 0.01$ and the prolongation was chosen as in (14), respecting the pattern condition (18). The factorization in Algorithm 1 was carried out, if the size of the coarsest grid (COARSEGRID) in the preconditioner-setup was below 800 for the tetrahedra and 1000 for the cube-models. The coarse system is solved by means of a Cholesky-factorization. It should be mentioned that the solver times for the tetrahedra model with a fixed value of COARSEGRID = 1000 were only slightly slower, so that this parameter could be fixed to 1000 for the considered resolution range.

Figure 9 shows a result of the FE calculations, achieved on two (9a) and 12 (9b) processors. The isopotential lines have been interpolated and visualized from $-5\mu V$ up to $5\mu V$ on an axial layer of the 2mm cube mesh (left) and from -1.6 to 0.7 μV on the surface of the tetrahedra head model (right). Note the blurring effect of the isolating skull-layer on the axial slice.

5.1 Realistic tetrahedra model

For the realistic tetrahedra model, the local accumulation of the geometry matrix K_s on 1 processor took 173.4 seconds, parallelized on 12 processors a setup time of 14.89 seconds was achieved.

Figure 10 shows the wall-clock time of the parallel AMG-CG solver compared to the parallel Jacobi-CG.

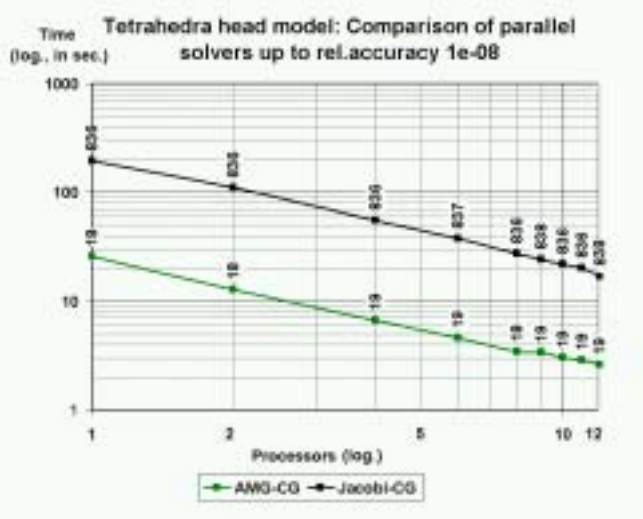

Figure 10. *SGI ORIGIN: Wall-clock time from 1 to 12 processors for the solver part of the parallel AMG-CG compared to the parallel Jacobi-CG up to an accuracy of* 10^{-8} *for the realistic tetrahedra head model, 118299 nodes. The numbers of iterations are shown over the curves.*

The number of iterations for both solvers, necessary for the required accuracy, is shown over the curves. The time for the setup of the preconditioner is not included, since it has to be carried out only once per head model and is thus neglectable with regard to the solution of the inverse problem. To give an impression, the setup of the AMG on 1 processor took 29.9 seconds and parallelized on 12 processors 7.4 seconds. The 3D potential distribution was calculated on one processor within 195.8 seconds with the Jacobi-CG method, whereas the parallel AMG-CG method on 12 processors needed 2.6 seconds. This is a factor of about 75 (7.5 through multigrid preconditioning and 10 through parallelization).

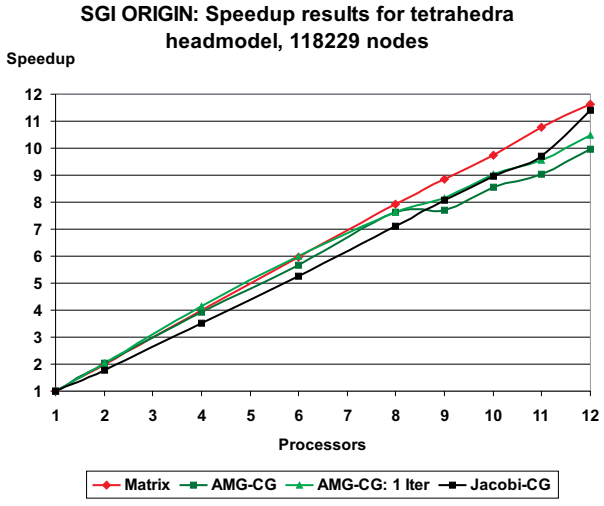

Figure 11. *SGI ORIGIN: Speedup results from 1 to 12 processors for the tetrahedra head model, 118299 nodes.*

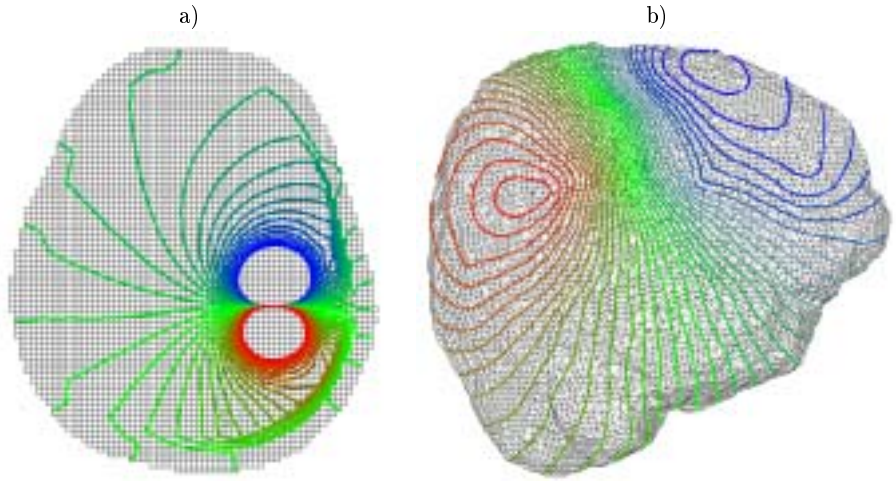

Figure 9. *Isopotential-lines: a) from -5 to 5 μV on an axial layer through the location of the source in the cube head model, calculated on 2 processors b) from -1.6 to 0.7 μV on the surface of the tetrahedra head model, calculated on 12 processors.*

The speedup results from 1 to 12 processors are shown in Figure 11. The matrix generation is purely local and gives the reference curve for the quasi optimal speedup. This curve can also be seen as an indicator for the quality of the mesh-partitioning, described in Subsection 3.2. The speedups for the parallel AMG-CG solver, for one iteration of this solver and for the parallel Jacobi-CG solver are compared.

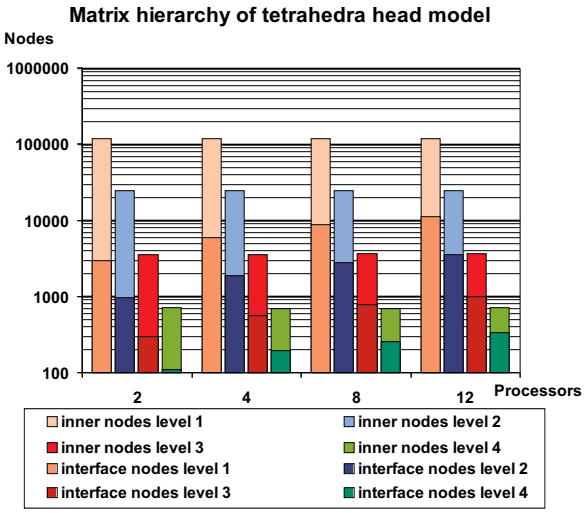

Figure 12. *Realistic tetrahedra head model, 118299 nodes: Relation interface nodes to all nodes (interface plus inner nodes) on the four levels of the algebraic multigrid, exemplarily for the decompositions for 2, 4, 8 and 12 processors.*

Since the coarsening process and the determination of the prolongation matrix $\mathfrak{P}$ respecting pattern condition (18) in the setup of the parallel AMG-preconditioner and the smoother-component of the solver depend on the decomposition into subdomains and a strongly increasing number of interface-nodes would spoil the preconditioning effect, it is interesting to have a look at the relation of interface nodes to all nodes (interface plus inner nodes) on the different levels of the multigrid. Figure 12 shows this relation exemplarily for 2, 4, 8 and 12 processors. The decomposition into two domains lead to 2986 and thus 2.5 % interface nodes on the finest level. On the third level (their is no more smoother component on the fourth and coarsest virtual grid), 294 out of 3581 nodes were interface nodes and thus a percentage of 8.2%. On 12 processors, 11175 and thus 9% were interface nodes on the finest level and on the third level, 998 out of 3675, i.e., 27%.

5.2 Realistic cube model

For the cube head model, the local geometry matrix accumulation took 183.2 seconds on 1 processor and parallelized on 12 processors 15.80 seconds.

Figure 13 shows the wall-clock time of the parallel AMG-CG solver compared to the parallel Jacobi-CG for the realistic cube model with 325384 nodes. Again, the number of iterations is shown over the curves. As for the tetrahedra-model, the time for the setup of the preconditioner is not included. The setup of the AMG for the cube model on 1 processor took 184 seconds and parallelized on 12 processors 29.6 seconds. The 3D potential distribution was calculated on one processor within 499 seconds with the Jacobi-CG method, whereas the parallel AMG-CG method on 12 processors needed 8.3 seconds. This is a factor of about 60 (6.3 through multigrid preconditioning and 9.5 through parallelization).

The speedup results from 1 to 12 processors are shown in Figure 14. Again, the matrix generation gives the reference curve for the quasi optimal speedup.

Let us have a closer look at the percentage of interface nodes to all nodes (interface plus inner nodes) on the five levels of the multigrid. Figure 15 shows this relation

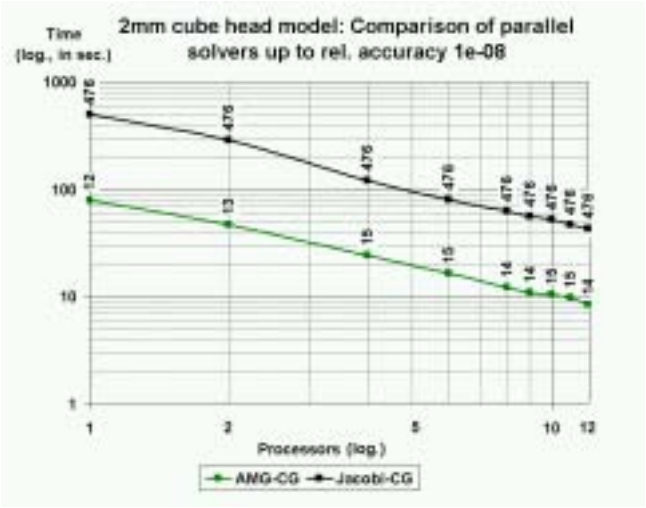

Figure 13. *SGI ORIGIN: Wall-clock time from 1 to 12 processors for the solver part of the parallel AMG-CG compared to the parallel Jacobi-CG up to an accuracy of* 10^{-8} *for the realistic cube head model, 325384 nodes. The numbers of iterations are shown over the curves.*

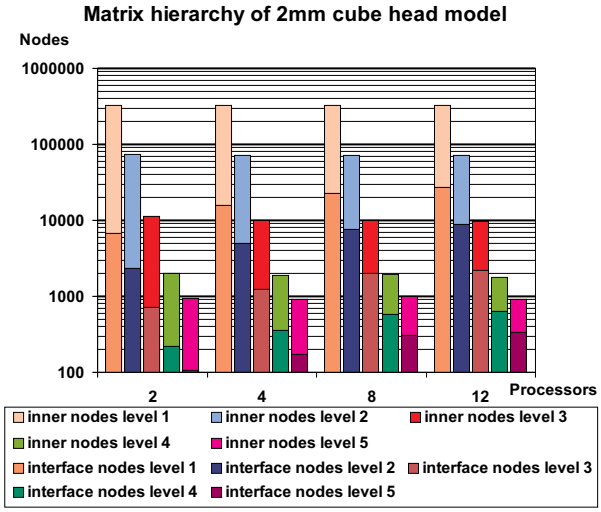

Figure 15. *Realistic cube head model, 325384 nodes: Relation interface nodes to all nodes (interface plus inner nodes) on the five levels of the algebraic multigrid, exemplarily for the decompositions for 2, 4, 8 and 12 processors.*

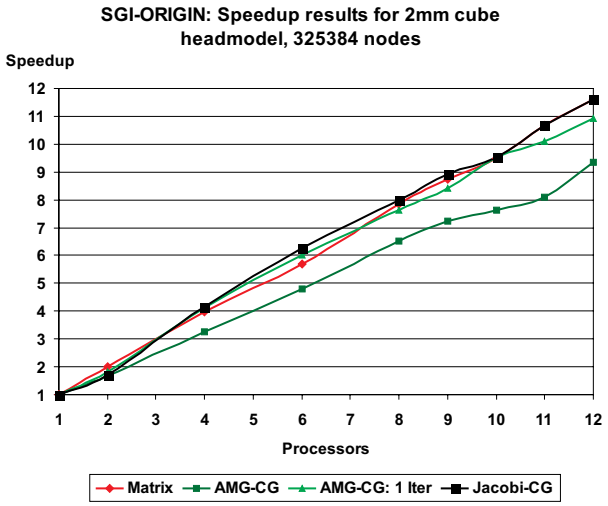

Figure 14. *SGI ORIGIN: Speedup results for 2mm cube head model, 325384 nodes, relative accuracy* 10^{-8}.

exemplarily for 2, 4, 8 and 12 processors. The decomposition into two domains lead to 6659 and thus 2% interface nodes on the finest level. On the fourth level, 219 out of 2029 nodes were interface nodes and thus a percentage of 10.8%. On 12 processors, 27312 and thus 8.4% were interface nodes on the finest level and on the third level, 637 out of 1804, i.e., 35.3%.

6 Discussion and Conclusions

High resolution FE head modeling allows the inclusion of head tissue conductivity inhomogeneities and anisotropies. Many studies indicate the necessity of such a complex forward model within EEG/MEG-based source localization methods. The bottleneck for a broader application is the time for solving the large linear equation system with thousands of different right hand sides arising from the FE discretization. Within this paper, an efficient and memory-economical way was presented to face this problem. Very short calculation times were achieved through the combination of AMG preconditioning techniques and the parallelization on distributed memory platforms.

We compared the presented AMG-CG with the Jacobi-CG, the latter being a well-known solver method in FE-based source localization. If the Jacobi-CG on a single processor is taken as a reference, we achieved a speedup of 75 for a realistically shaped high resolution tetrahedra head model with 118299 nodes when comparing to the parallel AMG-CG on 12 processors, 7.5 through multigrid preconditioning and 10 through parallelization on 12 processors. The factor for the realistically shaped high resolution cube model with 325384 nodes was 60, 6.3 through multigrid preconditioning and 9.5 through parallelization on 12 processors. On 12 processors, the parallel AMG-CG was a factor 6.6 faster than the parallel Jacobi-CG for the tetrahedra model and a factor 5.1 for the cube model. The required relative solution accuracy was 10^{-8}. For a solution accuracy of 10^{-6} with respect to the limitations within the inverse problem (e.g. data noise), we found factors in the same range (slightly larger).

The partitioning of the dual graph of a convex head geometry generally leads to a relatively large percentage of interface nodes. Nevertheless, for the examined moderate processor numbers between 1 and 12, the AMG-preconditioner was found to be stable, i.e., a sensible increase of the number of subdomains did not result in a deterioration of the AMG-preconditioner and thus an

increasing need for iterations for the tetrahedra model (Figure 10) or resulted in only a slight deterioration with a slightly increased number of iterations for the cube model (Figure 13).

In Wolters et al. [50] it was shown on a single processor machine that a radial:tangential "skull"-layer anisotropy of 1:10 in a spherical four layer FE model did not influence the solver times of the AMG-CG whereas the time for the Jacobi-CG solver was a factor 1.25 larger for the anisotropic models. This is due to the fact that the AMG-preconditioner takes anisotropy into account. Future studies will be carried out to test the sensitivity of the parallelized AMG-CG solver to realistic skull anisotropy and especially white matter anisotropy.

Moreover, the overall solver CPU-time for the inverse source reconstruction will be accelerated through the use of techniques for multiple right hand sides [10; 18]. First studies on a sequential computer have shown a good performance.

7 Note added in proof

The presented parallel AMG-CG solver was recently shown to be stable towards modeling of realistic conductivity anisotropy of the head compartments brain white matter and skull (see Wolters et al. [51]).

References

[1] M. Akhtari, H.C. Bryant, A.N. Marmelak, L. Heller, J.J. Shih, M. Mandelkern, A. Matlachov, D.M. Ranken, E.D. Best, and W.W. Sutherling. Conductivities of three-layer human skull. *Brain Top.*, 13(1):29–42, 2000.

[2] W. Andrä and H. Nowak. *Magnetism in medicine – a handbook.* Wiley–VCH, Berlin·Weinheim·New York·Chichester·Brisbane·Singapore·Toronto, 1998.

[3] K.A. Awada, D.R. Jackson, J.T. Williams, D.R. Wilton, S.B. Baumann, and A.C. Papanicolaou. Computational aspects of finite element modeling in EEG source localization. *IEEE Trans. Biomed. Eng.*, 44(8):736–751, 1997.

[4] P. Bastian, K. Birken, K. Johannsen, S. Lang, N. Neuss, H. Rentz-Reichert, and C. Wieners. UG – A flexible Software Toolbox for Solving Partial Differential Equations. *Comput. Vis. Sci.*, 1:27 – 40, 1997.

[5] O. Bertrand, M. Thévenet, and F. Perrin. 3D finite element method in brain electrical activity studies. In J. Nenonen, H.M. Rajala, and T. Katila, editors, *Biomagnetic Localization and 3D Modelling*, pages 154–171. Report of the Department of Technical Physics, Helsinki Univ. of Technology, 1991.

[6] D. Braess. Towards algebraic multigrid for elliptic problems of second order. *Computing*, 55:379–393, 1995.

[7] H. Buchner, G. Knoll, M. Fuchs, A. Rienäcker, R. Beckmann, M. Wagner, J. Silny, and J. Pesch. Inverse localization of electric dipole current sources in finite element models of the human head. *Electroenc. Clin. Neurophysiol.*, 102:267–278, 1997.

[8] S. Burkhardt, C.H. Wolters, and D. Saupe. Segmentation of human skull surfaces from bimodal MRI volumes. 2002. submitted to Med.Imag.Anal.

[9] CAUCHY. Anatomic source reconstruction of EEG/MEG-data. RWTH Aachen, Neurologie, 1997.

[10] T.F. Chan and W. L. Wan. Analysis of projection methods for solving linear systems with multiple right-hand sides. *SIAM J. Sci. Comput.*, 18(6):1698 – 1721, 1997.

[11] CURRY. Current reconstruction and imaging. NeuroScan Labs, http://www.neuro.com/ neuroscan/ prod05.htm, 2000.

[12] J.C. de Munck and M. Peters. A fast method to compute the potential in the multi sphere model. *IEEE Trans. Biomed. Eng.*, 40(11):1166–1174, 1993.

[13] R. Falgout, Van E. Henson, J. E. Jones, and U. Meier Yang. Boomer AMG: A parallel implementation of algebraic multigrid. Techn. Report UCRL-MI-133583, Lawrence Livermore National Laboratory, March 1999.

[14] M. Fuchs, M. Wagner, H.A. Wischmann, T. Köhler, A. Theißen, R. Drenckhahn, and H. Buchner. Improving source reconstructions by combining bioelectric and biomagnetic data. *Electroenc. Clin. Neurophysiol.*, 107:93–111, 1998.

[15] G. Haase. *Parallelisierung numerischer Algorithmen für partielle Differentialgleichungen.* B.G.Teubner, Stuttgart·Leipzig, 1999.

[16] G. Haase, M. Kuhn, and S. Reitzinger. Parallel AMG on distributed memory computers. *SIAM J. Sci.Comp.*, 2002. in press.

[17] G. Haase, U. Langer, S. Reitzinger, and J. Schöberl. A general approach to algebraic multigrid. Technical Report 00-33, J. Kepler Univ. Linz, SFB "Numerical and Symbolic Scientific Computing", 2000.

[18] G. Haase and S. Reitzinger. Algebraic multigrid methods for linear systems with multiple right-hand sides. Technical Report 02-5, Johannes Kepler University Linz, SFB "Numerical and Symbolic Scientific Computing", 2002.

[19] W. Hackbusch. *Multigrid Methods and Application.* Springer Verlag, 1985.

[20] J. Haueisen. *Methods of Numerical Field Calculation for Neuromagnetic Source Localization.* PhD thesis, Technical Univ.Ilmenau, 1996.

[21] J. Haueisen, D.S. Tuch, C. Ramon, P. Schimpf, and H. Nowak. Conductivity tensor information in a 3D finite element model of the human head for MEG and EEG forward computations. *NeuroImage, 4th International Hans Berger Congress, Sept. 26–29*, 10(3):A2, 1999.

[22] G. Huiskamp, M. Vroeijenstijn, R. van Dijk, G. Wieneke, and A.C. van Huffelen. The need for correct realistic geometry in the inverse EEG problem. *IEEE Trans. Biomed. Eng.*, 46(11):1281–1287, 1999.

[23] C.R. Johnson, M. Mohr, U. Rüde, A. Samsonov, and K. Zyp. Multilevel methods for inverse bioelectric field problems. In R. Bank, T. Barth, and T. Chan, editors, *Yosemite Educational Symposium*, http://raphael.mit.edu/yosemite/, Oct.29–Nov.1, 2000.

[24] M. Jung and U. Langer. Applications of multilevel methods to practical problems. *Surv.Math.Ind.*, 1:217–257, 1991.

[25] G. Karypis and V. Kumar. METIS – User's Guide. University of Minnesota, http://www-users.cs.umn.edu/ ~karypis, 1998.

[26] F. Kickinger. Algebraic multigrid for discrete elliptic second-order problems. In W. Hackbusch, editor, *Multigrid Meth. V. Proc. of the 5th Europ. Multigrid conf.*,

pages 157–172. Springer Lect. Notes Comput. Sci. Eng. 3, 1998.

[27] T.R. Knösche. *Solutions of the neuroelectromagnetic inverse problem*. PhD thesis, Univ. of Twente, The Netherlands, 1997.

[28] A. Krechel and K. Stüben. Parallel algebraic multigrid based on subdomain blocking. *Parallel Comp.*, 27(8):1009 – 1031, 2001.

[29] B. Maess, S. Koelsch, T.C. Gunter, and A.D. Friederici. Musical syntax is processed in broca's area: an MEG study. *Nature Neuroscience*, 4(5):540–545, 2001.

[30] G. Marin, C. Guerin, S. Baillet, L. Garnero, and Meunier G. Influence of skull anisotropy for the forward and inverse problem in EEG: simulation studies using the FEM on realistic head models. *Human Brain Mapping*, 6:250–269, 1998.

[31] P.L. Nunez. Localization of brain activity with electroencephalography. In S. Sato, editor, *Magnetoencephalography*, pages 39–65. Raven Press, New York, 1990.

[32] B.U. Öztekin, G. Karypis, and V. Kumar. PMVIS – User's Guide. University of Minnesota, http://www-users.cs.umn.edu/ ∼oztekin/ pmvis/, 1998.

[33] W. Platzer, editor. *Pernkopf Anatomie*. Urban & Schwarzenberg, München, 1994.

[34] R. Plonsey and D. Heppner. Considerations on quasi-stationarity in electro-physiological systems. *Bull.math.Biophys.*, 29:657–664, 1967.

[35] R. Pohlmeier, H. Buchner, G. Knoll, A. Rienäcker, R. Beckmann, and J. Pesch. The influence of skull-conductivity misspecification on inverse source localization in realistically shaped finite element head models. *Brain Top.*, 9(3):157–162, 1997.

[36] S. Reitzinger. PEBBLES – User's Guide. SFB F013 "Numerical and Symbolic Scientific Computing", http://www.sfb013.uni-linz.ac.at., 1999.

[37] J. W. Ruge and K. Stüben. Algebraic multigrid (AMG). In S. McCormick, editor, *Multigrid Methods*, volume 5 of *Frontiers in Applied Mathematics*, pages 73–130. SIAM, Philadelphia, 1986.

[38] M. Scherg and D. von Cramon. Two bilateral sources of the late AEP as identified by a spatio-temporal dipole model. *Electroenc. Clin. Neurophysiol.*, 62:32–44, 1985.

[39] U. Schmitt and A.K. Louis. Efficient algorithms for the regularization of dynamic inverse problems: I.theory. *Inverse Problems*, 18(3):645–658, 2002.

[40] U. Schmitt, A.K. Louis, C.H. Wolters, and M. Vauhkonen. Efficient algorithms for the regularization of dynamic inverse problems: II.applications. *Inverse Problems*, 18(3):659–676, 2002.

[41] SimBio. A generic environment for bio-numerical simulation. IST-program of the European Commission, Project No.10378, http://www.simbio.de, 2000.

[42] W.R. Smythe. *Static and dynamic electricity*. Hemisphere Publishing, New York, 1989.

[43] W.W. Sutherling, P.H. Crandall, T.M. Darcey, D.P. Becker, M.F. Levesque, and D.S. Barth. The magnetic and electrical fields agree with intracranial localizations of somatosensory cortex. *Neurology*, 38:1705–1714, 1988.

[44] D.S. Tuch, V.J. Wedeen, A.M. Dale, and J.W. Belliveau. Electrical conductivity tensor map of the human brain using NMR diffusion imaging: An effective medium approach. *ISMRM, 6th Scientific Meeting, Sydney*, 1998.

[45] S.P. van den Broek, M. Donderwinkel, and M.J. Peters. The influence of inhomogenities in a realistically shaped volume conductor on EEG and MEG. In H. Witte, U. Zwiener, B. Schack, and A. Doering, editors, *Quantitative and Topological EEG and MEG Analysis*, pages 456–458. Druckhaus Mayer Verlag GmbH Jena · Erlangen, 1997.

[46] T.D. Waberski, H. Buchner, K. Lehnertz, A. Hufnagel, M. Fuchs, R. Beckmann, and A. Rienäcker. The properties of source localization of epileptiform activity using advanced headmodelling and source reconstruction. *Brain Top.*, 10(4):283–290, 1998.

[47] C. Wagner. On the algebraic construction of multilevel transfer operators. *Computing*, 65:73–95, 2000.

[48] M. Wagner. *Rekonstruktion neuronaler Ströme aus bioelektrischen und biomagnetischen Messungen auf der aus MR-Bildern segmentierten Hirnrinde*. PhD thesis, Shaker-Verlag Aachen, 1998.

[49] C. Wolters. *Influence of tissue conductivity inhomogeneity and anisotropy to EEG/MEG based source localization in the human brain*. PhD thesis, University of Leipzig, 2002. in preparation.

[50] C. Wolters, S. Reitzinger, A. Basermann, S. Burkhardt, U. Hartmann, F. Kruggel, and A. Anwander. Improved tissue modeling and fast solver methods for high resolution FE-modeling in EEG/MEG-source localization. In J. Nenonen, R.J. Ilmoniemi, and T. Katila, editors, *Proc. of the 12th Int.Conf.of Biomagnetism*, pages 655–658, http://biomag2000.hut.fi/papers_all.html, Aug.13–17, 2000.

[51] C.H. Wolters, A. Anwander, M. Koch, S. Reitzinger, M. Kuhn, and M. Svénsen. Influence of head tissue conductivity anisotropy on human EEG and MEG using fast high resolution finite element modeling, based on a parallel algebraic multigrid solver. In T. Plesser and P. Wittenburg, editors, *Forschung und wissenschaftliches Rechnen·Heinz-Billing Award for the Advancement of Scientific Computing*, http://www.mpg.de/billing/, 2002. Gesellschaft für wissenschaftliche Datenverarbeitung mbH Göttingen.

[52] C.H. Wolters, R.F. Beckmann, A. Rienäcker, and H. Buchner. Comparing regularized and non-regularized nonlinear dipole fit methods: A study in a simulated sulcus structure. *Brain Top.*, 12(1):3–18, 1999.

[53] C.H. Wolters, U. Hartmann, M. Koch, F. Kruggel, S. Burkhardt, A. Basermann, D.S. Tuch, and J. Haueisen. New methods for improved and accelerated FE volume conductor modeling in EEG/MEG-source reconstruction. In J. Middleton, M. Jones, N. Shrive, and G. Pande, editors, *4th Symp. on Computer Methods in Biomech. and Biomed.Eng.*, pages 489–494, Lisboa, Okt.31–Nov.3 1999. Gordon & Breach.

[54] F. Zanow and M.J. Peters. Individually shaped volume conductor models of the head in EEG source localisation. *Med. & Biol. Eng. & Comput.*, 7:151–161, 1995.